Xue *et al. Chin. J. Mech. Eng.* (2021) 34:80
https://doi.org/10.1186/s10033-021-00596-x

Chinese Journal of Mechanical Engineering

ORIGINAL ARTICLE

Open Access

HAZ Characterization and Mechanical Properties of QP980-DP980 Laser Welded Joints

Junliang Xue[1], Peng Peng[1], Wei Guo[1*], Mingsheng Xia[2], Caiwang Tan[3], Zhandong Wan[4], Hongqiang Zhang[1] and Yongqiang Li[5]

Abstract

The QP980-DP980 dissimilar steel joints were fabricated by fiber laser welding. The weld zone (WZ) was fully martensitic structure, and heat-affected zone (HAZ) contained newly-formed martensite and partially tempered martensite (TM) in both steels. The super-critical HAZ of the QP980 side had higher microhardness (~ 549.5 Hv) than that of the WZ due to the finer martensite. A softened zone was present in HAZ of QP980 and DP980, the dropped microhardness of softened zone of the QP980 and DP980 was Δ 21.8 Hv and Δ 40.9 Hv, respectively. Dislocation walls and slip bands were likely formed at the grain boundaries with the increase of strain, leading to the formation of low angle grain boundaries (LAGBs). Dislocation accumulation more easily occurred in the LAGBs than that of the HAGBs, which led to significant dislocation interaction and formation of cracks. The electron back-scattered diffraction (EBSD) results showed the fraction of LAGBs in sub-critical HAZ of DP980 side was the highest under different deformation conditions during tensile testing, resulting in the failure of joints located at the sub-critical HAZ of DP980 side. The QP980-DP980 dissimilar steel joints presented higher elongation (~ 11.21%) and ultimate tensile strength (~ 1011.53 MPa) than that of DP980-DP980 similar steel joints, because during the tensile process of the QP980-DP980 dissimilar steel joint (~ 8.2% and 991.38 MPa), the strain concentration firstly occurred on the excellent QP980 BM. Moreover, Erichsen cupping tests showed that the dissimilar welded joints had the lowest Erichsen value (~ 5.92 mm) and the peak punch force (~ 28.4 kN) due to the presence of large amount of brittle martensite in WZ and inhomogeneous deformation.

Keywords: QP980 steel, DP980 steel, Fiber laser welding, Microstructure evolution, Tensile properties, Formability

1 Introduction

In order to reduce the weight of automobiles and increase requirement of passenger safety, advanced high strength steels (AHSSs) have been widely applied in automotive industry [1, 2]. Currently, the third generation AHSSs via a novel heat treatment processing, "quenching and partitioning" (QP), have drawn much attention because of their low-cost and superior combination of strength and ductility [3, 4]. The retained austenite (RA) in QP steel can transform into martensite during deformation due to the transformation-induced plasticity effect (the TRIP effect) [5, 6], which decelerates the propagation of crack and enhances the strength and uniform elongation [7].

During the manufacturing processes, jointing of dissimilar or similar AHSSs using fusion welding techniques is inevitable [8]. However, heat input of fusion welding of AHSSs is associated with some problems such as heat affected zone (HAZ) softening, formation of porosities as well as solidification cracks. Guzman-Aguilera et al. [9] assessed the effect of the welding heat input on the microstructure and mechanical properties of Si-alloyed TRIP steel. They found that the welded joints occurred softening at the sub-critical HAZ and the failure location of the arc welded samples was the sub-critical HAZ. Farabi et al. [10] suggested that the degree of softening was

*Correspondence: gwei@buaa.edu.cn
[1] School of Mechanical Engineering and Automation, Beihang University, Beijing 100191, China
Full list of author information is available at the end of the article

Table 1 Chemical compositions (wt.%) of the BM

Steels	C	Mn	Si	Al	Cr	Mo	Fe
QP980	0.2	2.41	1.31	0.06	0.04	–	Bal.
DP980	0.15	1.5	0.31	0.05	0.02	0.05	Bal.

more obvious in DP980 than DP600 during laser welding, and tensile failure was in the soft zone of DP600 side. Li et al. [11] studied the tensile properties and formability of laser welding joints of QP980, showing that the microhardness of the sub-critical heat affected zone (HAZ) decreased due to martensite tempering. In addition, the formability ratio was only 68.08% of QP980 base material (BM) in Erichsen cupping test. Conclusively, the HAZ of welded joints had a negative effect.

Compared with conventional welding methods, laser welding is becoming popular in manufacturing auto-body parts due to its high energy density, excellent welded quality and rapid welding speed [12–14]. Guo et al. [15] found all the laser welded joints failed at base metal during quasi-static and dynamic tensile tests. And the laser welding can reduce welding heat input, leading to a narrower HAZ and improved mechanical and formability properties of the joints [16, 17].

The dissimilar AHSSs welded joints can achieve light weight and maximal material efficiency. DP steel consists of hard martensite islands embedded in the soft ferrite matrix which increases strength and ductility [18]. And DP steel has been widely used in motor vehicles [19, 20]. Consequently, the dissimilar AHSSs welded joints, especially QP and DP steel joints are important in industrial applications. Nevertheless, few studies have been carried out on the influence of HAZ on mechanical properties of dissimilar QP-DP welded joints.

The purpose of this study was to investigate the effect of the HAZ, especially softened zone, on mechanical properties of fiber laser welded QP980 and DP980 dissimilar joints. Microstructure, microhardness, tensile properties and biaxial stretch formability were studied. The microstructure evolution of the softened zone of QP980 and DP980 under different strain was compared by electron back-scattered diffraction (EBSD).

2 Experimental Procedure

2.1 Materials and Laser Welding

1.35 mm thick QP980 steel sheet and DP980 steel sheets were used. Their chemical compositions were shown in Table 1. Welded blanks with a dimension of 100 mm × 200 mm were fabricated by laser butt welding using IPG Photonics YLS-6000 fiber laser system. Figure 1 shows the schematic illustration of laser welding. During laser welding, the welding direction was perpendicular to the rolling direction of base material, and laser welding parameters are listed in Table 2.

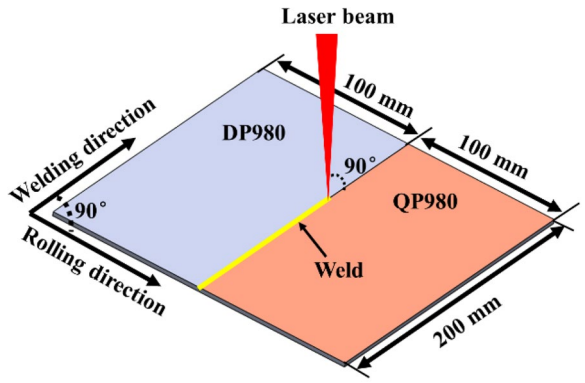

Figure 1 Schematic diagram of laser welding

Table 2 Parameters of laser welding

Laser power (kW)	Welding speed (m/min)	Focal length (cm)	Beam dimension (mm)	Head angle (°)
4.5	8	30	0.6	0

2.2 Microstructure Characterization

Metallographic specimens were cut from the center of welded joint and then mounted, ground, polished, and etched with 3% Nital solution. Optical microscope (OM, Zeiss Scope.A1), scanning electron microscope (SEM, Merlin Compact) and EBSD were used to characterize the microstructural evolution. Specimens for EBSD were mechanical polished, and then electro-polished for stress relieving using a solution of 15 mL perchloric acid and 285 mL alcohol at 20 V for 20 s. Image quality (IQ) map, inverse pole figure (IPF) map, Kernel average misorientation (KAM) map and Taylor Factor (TF) map can be obtained by EBSD. The family of active slip systems for BCC metals (< 1 −1 1>) was used to get Taylor factors and deformation gradient for uniaxial tension (Eq. (1)) [21]

$$\boldsymbol{F} = \begin{bmatrix} 1 & 0 & 0 \\ 0 & -0.5 & 0 \\ 0 & 0 & -0.5 \end{bmatrix}. \quad (1)$$

Vickers microhardness of the welded joint was measured using a Vickers hardness tester (FM 800) with a 300 g load and 15 s dwell time.

2.3 Mechanical Properties and Erichsen Cupping Tests

The tensile specimens were machined according to ASTM: E8M, with a gauge length of 25 mm, gauge width of 6 mm (Figure 2a), the tensile direction was parallel to rolling direction. Erichsen cupping test was carried out with a standard of GB4156-84 at a constant speed of 10 mm/min. The Erichsen cupping test geometry as shown Figure 2b. The tensile tests were carried out by an electromechanical universal testing machine (MTSC45105) equipped with digital image correlation (DIC CSI VIC-2D) system under a constant speed of 1.5 mm/min, as shown in Figure 3. The fracture morphologies after tensile test and Erichsen cupping test were observed by SEM.

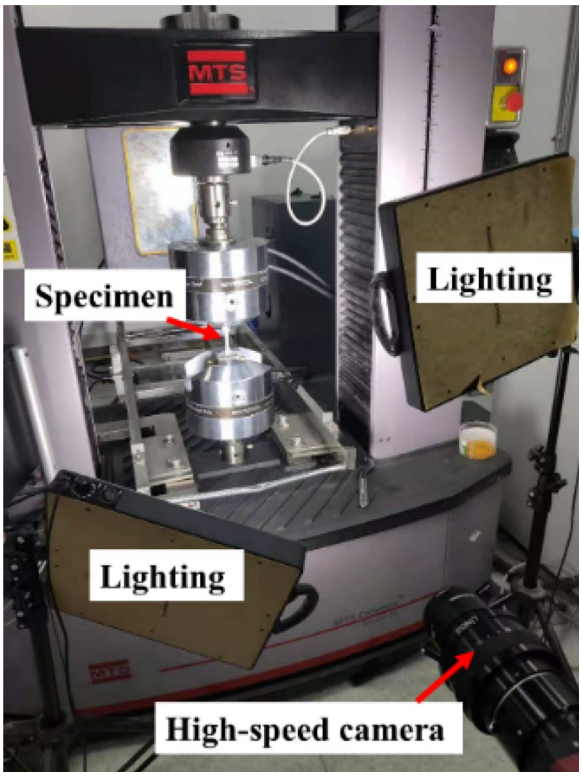

Figure 3 Electromechanical universal testing machine equipped with DIC system

3 Results and Discussion

3.1 Microstructure

The SEM and image quality (IQ) maps in EBSD of QP980 and DP980 steel are shown in Figure 4. The microstructure of QP980 in Figure 4a and b was comprised of ferrite, martensite and retained austenite (RA). Although ferrite and martensite both are difficult to distinguish by phase map because of their body centered cubic (BCC) α crystal structure [22], martensite islands are dark grains, as shown Figure 4b, owing to its faint Kikuchi patterns due to its highly distorted lattice compared with ferrite. Therefore, RA, face centered cubic (FCC) γ crystal structure, was marked with red color (Figure 4b). And the volume fraction of RA in QP980 was about 8.7%, while DP980 mainly consist of martensite and ferrite, as shown Figure 4c and d.

After fiber laser welding, the QP980-DP980 joints had no cracks and voids. The cross-sectional microstructure of joint can be identified as weld zone (WZ), HAZ and BM (Figure 5a). Because the cooling rate of the WZ was much higher than the critical forming rate of martensite, the WZ was fully martensite, as shown in Figure 5b. The HAZ of QP980 and DP980 sides could be divided three sub-regions, namely super-critical HAZ (Figure 5c and f), inter-critical HAZ (Figure 5d and g) and sub-critical HAZ (Figure 5e and h), according to the experienced different peak temperatures during laser welding. The super-critical HAZ of QP980 and DP980 sides (Figure 5c and f) experienced peak temperature above Ac_3 temperature, resulting in the original microstructure of BM was completely austenitized and then transformed to martensite upon a high cooling rate. The peak temperature in the inter-critical HAZ was between Ac_1 and Ac_3

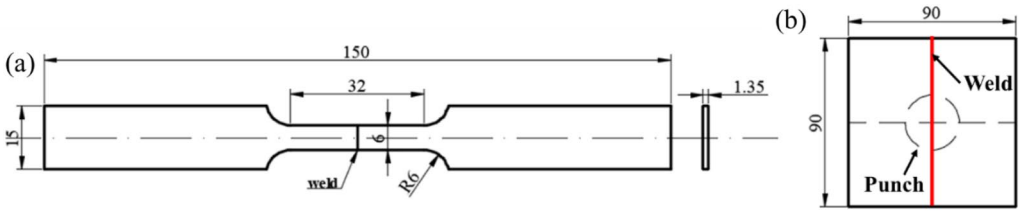

Figure 2 **a** Tensile specimen geometry (mm), **b** Erichsen cupping test geometry (mm)

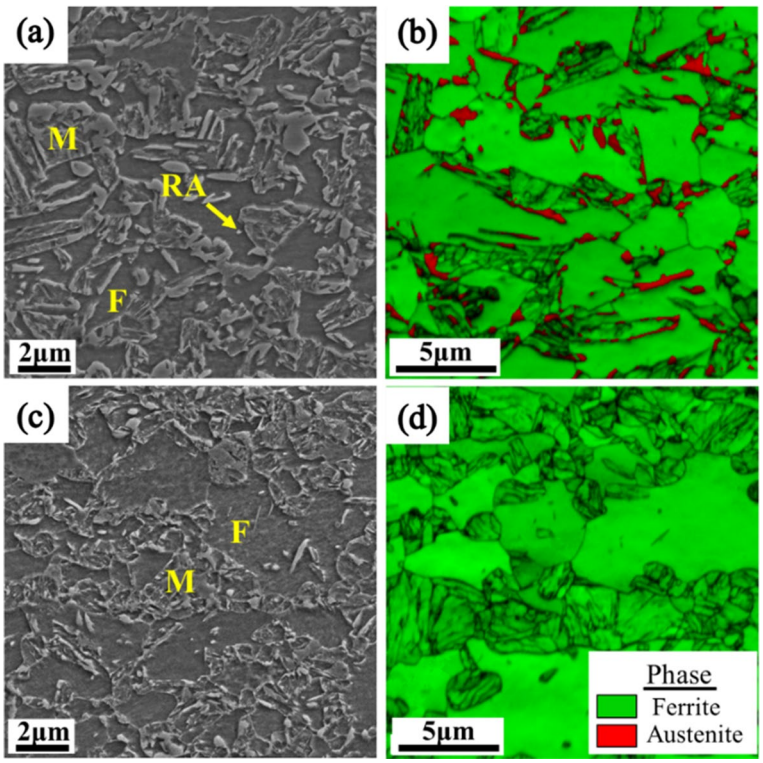

Figure 4 SEM and IQ map with phase of base materials: **a**, **b** QP980, and **c**, **d** DP980 (F: Ferrite; M: Martensite; RA: Retained Austenite)

lines, leading a partially austenitization. Consequently, the inter-critical HAZ contained martensite and ferrite as shown in Figure 5d and g. The peak temperature in sub-critical HAZ was below Ac_1 line, forming tempered martensite (TM) as displayed in Figure 5e and h. Hence, the sub-critical HAZ of QP980 consisted of tempered martensite, ferrite and a small portion of retained austenite. And the sub-critical HAZ of DP980 contained tempered martensite and ferrite.

3.2 Microhardness

Microhardness measurements are shown in Figure 6. For comparison, microhardness profiles of similar joints of QP980-QP980 and DP980-DP980 are also shown. It indicates that the microhardness was clearly different in different zones. The microhardness value of dissimilar joint exhibited an asymmetric characteristic with a higher hardness on the QP980 side and a lower hardness on the DP980 side (Figure 6a). The average hardness of QP980 and DP980 is 369.8 Hv and 298.9 Hv, respectively. All the WZ had the higher microhardness value than that of BM since the WZ was fully martensitic microstructure. Nevertheless, the microhardness of QP980 WZ was higher than that of DP980 WZ, due to the higher C content of the former [23].

The super-critical HAZ experienced a relatively low peak temperature (exceeded A_{C3}) with limited time. This condition could not promote austenite grow, thus fine martensite was generated with higher hardness than that of WZ. Thus, the super-critical HAZ of QP980 side had peak microhardness value of 549.5 Hv. And the super-critical HAZ of DP980 side also had higher microhardness than that of the WZ of near the DP980, similar result was presented in Ref. [11]. A significantly softened zone can be observed in sub-critical HAZ of QP980 (~21.8 Hv hardness drop than that of QP980 BM) and DP980 (~40.9 Hv hardness drop than that of DP980 BM) because of the tempering of martensite. In general, martensite tempering is an unavoidable phenomenon among AHSSs consisting of martensite phase. It depends on the volume fraction of martensite, the heat input and thermal properties [15, 24, 25]. Figure 6b shows the microhardness mapping of the entire cross section of the QP980-DP980 welded joint. The microhardness distribution in the vertical direction was consistent.

3.3 Tensile Properties

Seven typical deformation stages of unloaded, elastic deformation, uniform plastic deformation-1, uniform plastic deformation-2, maximum load, localized necking,

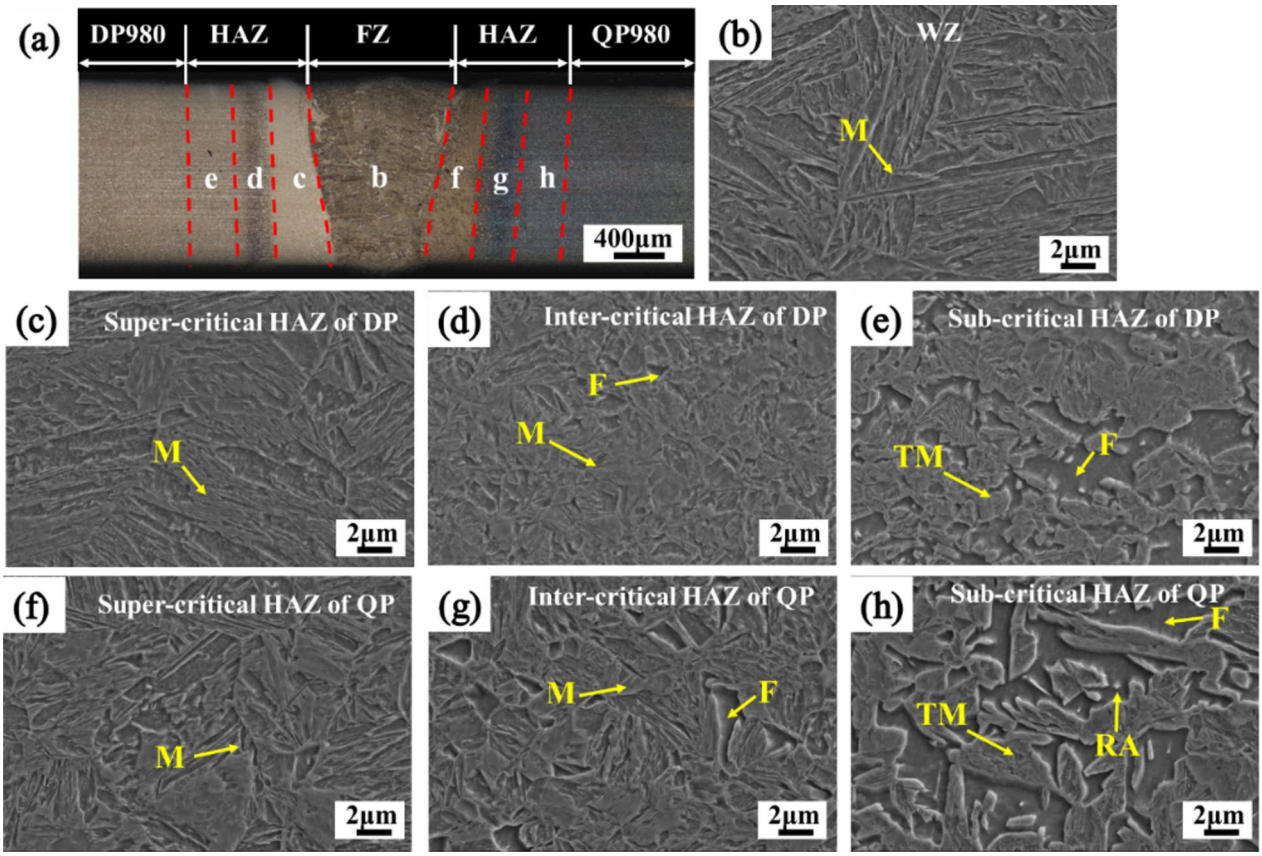

Figure 5 Microstructure of QP980-DP980 weld joint: **a** overview of the joint, **b** weld zone, DP980 of **c** super-critical HAZ, **d** inter-critical HAZ and **e** sub-critical HAZ; QP980 of **f** super-critical HAZ, **g** inter-critical HAZ and **h** sub-critical HAZ (F: ferrite; M: martensite; TM: tempered martensite; RA: retained austenite)

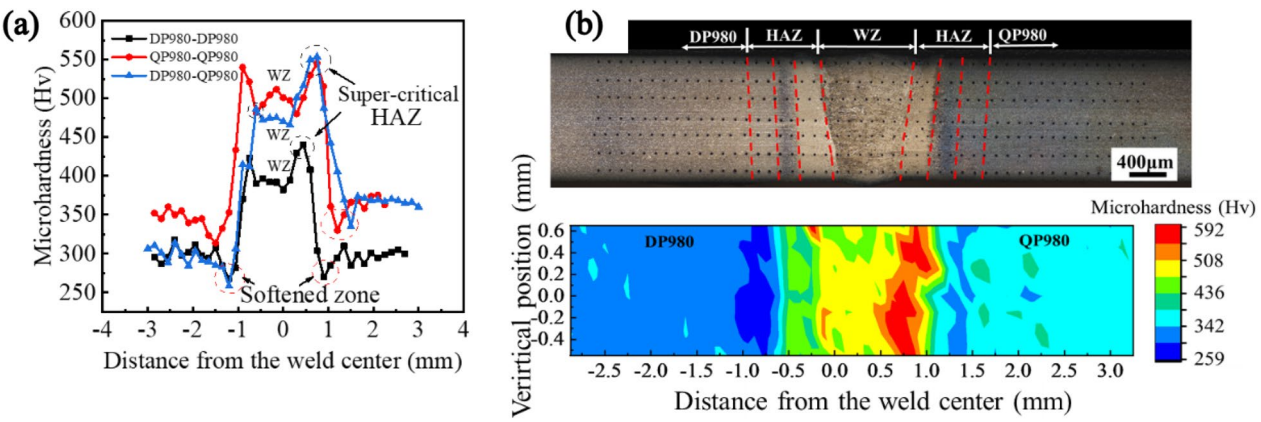

Figure 6 Microhardness profile across the welded joint: **a** typical hardness distribution, **b** hardness map of QP980-DP980 welded joint

and onset of fracture were selected using DIC, as shown Figure 7. The welded joints are indicated by solid lines, and the fracture location are marked by dash lines. The local axial strain along gauge length direction (red solid lines) at various strain stages were extracted and plotted in the right side of Figure 7.

In QP980-DP980 joint (Figure 7a), the strain concentration firstly occurred on the QP980 BM and then the

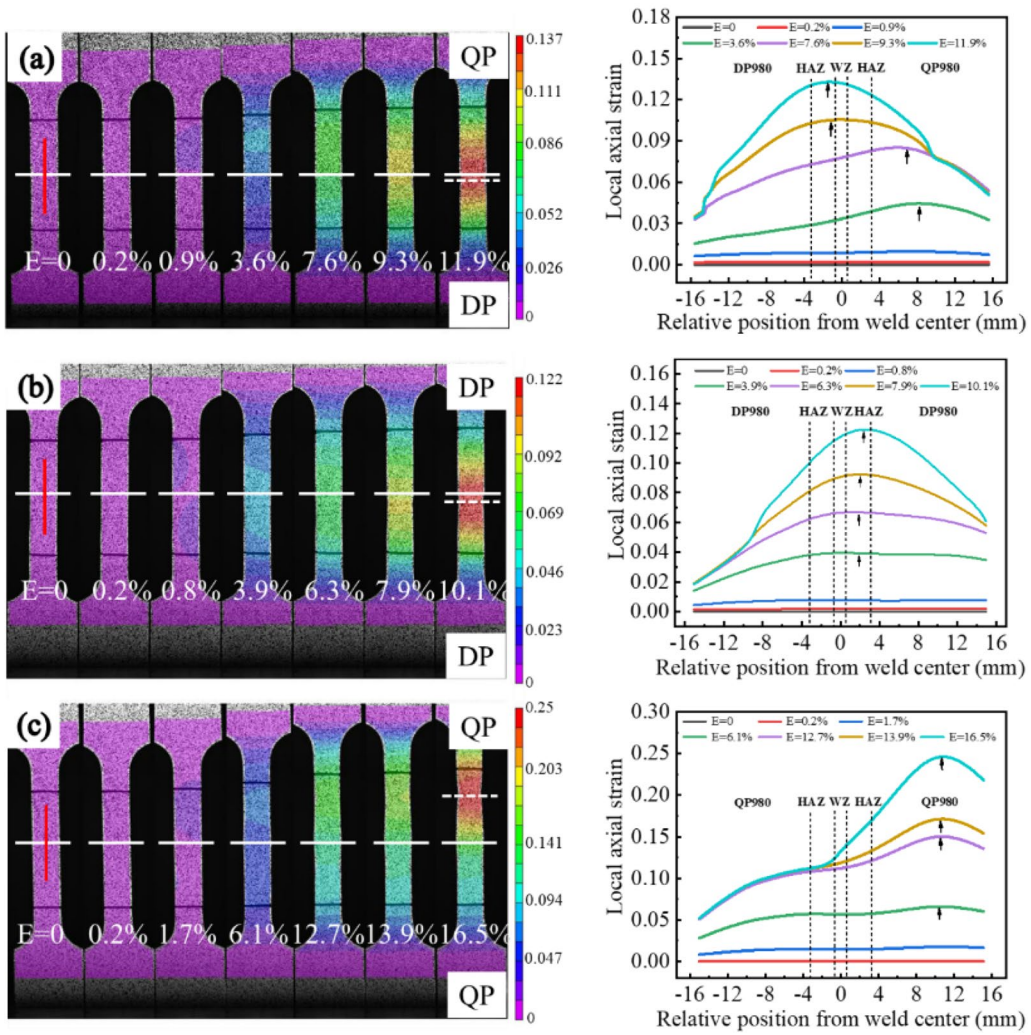

Figure 7 DIC measurement of strain maps and associated local axial strain profile at different loading stages for the joints: **a** QP-DP joint, **b** DP-DP joint, **c** QP-QP joint

maximum strain concentration transferred from the QP980 BM to the HAZ of DP980 side with the increase of strain. For the DP980-DP980 joint (Figure 7b), deformation was localized in both sides of the weld at the beginning, then localized in the HAZ. The localized necking appeared at the HAZ of DP980 side in both QP980-DP980 and DP980-DP980 joints after the stress reached the maximum value, and then specimens fractured in this necking region. The reason was that the HAZ included sub-critical HAZ (i.e., softened zone), and the sub-critical HAZ of the DP980 side had the worst mechanical properties [26]. Compared with QP980-DP980 and DP980-DP980 joints, the strain of QP980-QP980 joint (Figure 7c) always concentrated in the QP980 BM during tensile testing. Localized necking and fracture position also appeared the strain concentration area of the QP980 BM, as shown Figure 8c. From Figure 8a and b, the QP980-DP980 and DP980-DP980 joints failed at the soften zone of DP BM. Moreover, the ultimate tensile strength (UTS) and the YS of QP980-QP980 joints was not degraded. Thereby the sub-critical HAZ of QP980 side had a negligible effect on tensile testing [11, 15].

The engineering stress-strain curves of the QP980-DP980 joint, QP980-QP980 joint, DP980-DP980 joint, QP980 BM and DP980 BM are presented in Figure 9a. The details of tensile properties of BM and joints are given in Table 3. The UTS (1011.53 MPa) and elongation (11.21%) of QP980-DP980 joint are significantly higher than that of DP980-DP980 joint (991.38 MPa, 8.2%). But the UTS and elongation of QP980-DP980 joint are

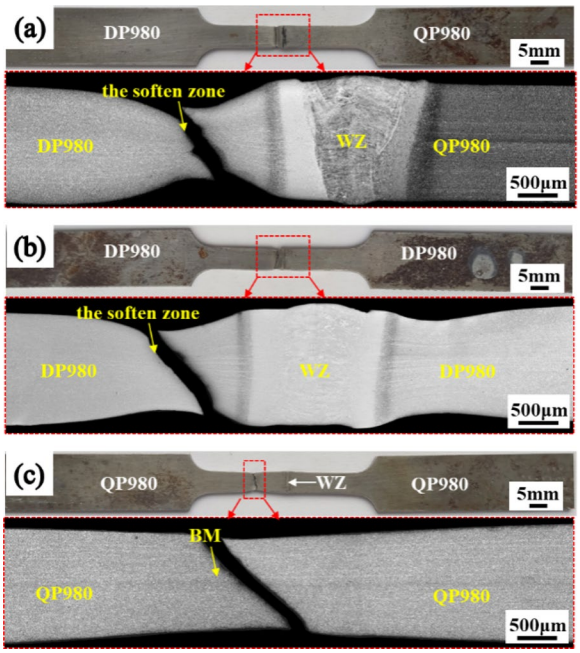

Figure 8 The fractured tensile sample: **a** QP-DP joint, **b** DP-DP joint, **c** QP-QP joint

obviously lower than that of QP980 BM (1072.07 MPa, 25.69%) and DP980 BM (1020.09 MPa, 16.54%). In addition, all the welded joints show a higher YS than those of the BM because of the hardened WZ [27].

According to DIC measurement, the strain of specimen concentrated invariably in the QP980 BM before the QP980-DP980 joints necked due to its low strength of QP980 BM during uniform plastic deformation stage, as shown enlarged drawing of Figure 9a. And the TRIP effect of RA in the QP980 BM made the QP980-DP980 joints possess better the tensile properties (such as UTS, YS, elongation and energy absorption) than DP980-DP980 welded joints.

According to the following equation, the true stress-strain curves and work hardening rate-true strain can be depicted (Figure 9b).

$$S = (1 + \varepsilon) \times \sigma, \tag{2}$$

$$e = \ln(1 + \varepsilon), \tag{3}$$

$$K = \frac{\mathrm{d}S}{\mathrm{d}e}, \tag{4}$$

where S is the true stress; e is the true stain; σ is the engineering stress; ε is the engineering strain; K is the work hardening rate.

The work hardening rate curves of the welded joints can be divided into two stages.

In stage 1 ($e < 0.025$), the work hardening rate of all the BM and joints rapidly decreased with the increase of the true strain, which is related to a sufficient dislocation movement [28]. The joints were elastically deformed or at the beginning of plastic deformation, indicating that all of the joints had an equal elasticity in small strain stage. In stage 2 ($e > 0.025$), a large number of dislocation

Table 3 Tensile properties of BM and joints

Material	UTS (MPa)	YS (MPa)	Elongation (%)	Energy absorption (GP %)
DP BM	1020.09	664.16	16.54	15.49
QP BM	1072.07	689.12	25.69	26.47
QP-DP	1011.53	708.92	11.21	10.1
DP-DP	991.38	698.82	8.2	7.38
QP-QP	1045.53	715.58	19.12	19.17

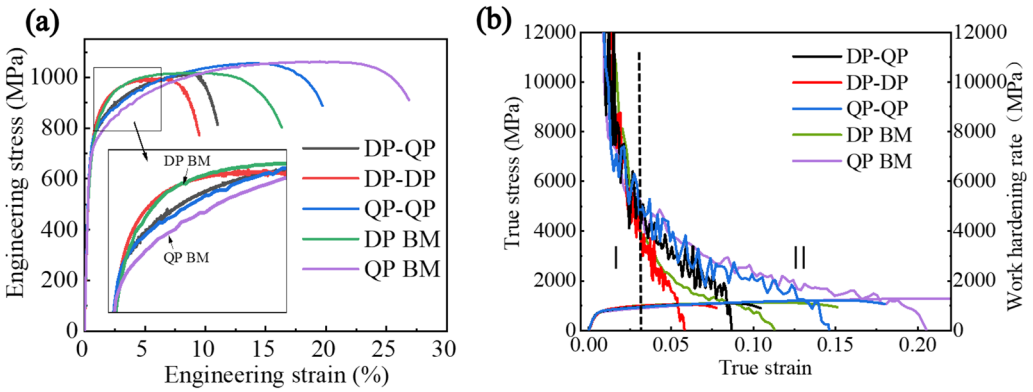

Figure 9 Tensile properties of base materials and joints: **a** engineering stress-strain curves, **b** true stress-strain curves and work-hardening rate curves

multiplication led to a stronger increase in dislocations density during plastic deformation process. Therefore, the movement of dislocation was prevented and the work hardening rate decrease slowly [29–31]. The decrease of the work hardening rate of QP980-QP980 and QP980-DP980 joints were slow because of the contribution of the TRIP effect caused by retained austenite [31, 32].

The micrograph of the fracture surface of joints and BM are exhibited in Figure 10. A large amount of dimples was observed on the fracture surface, representing a typical ductile fracture [33]. However, the fracture surface of QP980-DP980 and DP980-DP980 joints showed shallow dimples, as shown Figure 10c and d, suggesting a poor ductility caused by the softened zone of DP980 [22].

3.4 Microstructure Analysis under Different Strains

It was found that the sub-critical HAZ of DP side was the weakest zone of all joints during tensile testing. This section illustrates microstructural features of different zone by EBSD analysis. Firstly, image quality (IQ) maps with phase of different zone were created, as shown Figure 11a–d. The low angle grain boundaries (LAGB) with misorientation $2° < \theta < 10°$ were marked by green lines and the high angle grain boundaries (HAGB) with misorientation $\theta > 10°$ were delineated by blue lines. Generally, the fraction of LAGBs (f_{LAGBs}) is related with motion of dislocation; additionally, the motion, rearrangement and annihilation of dislocation are related to the strain during tensile testing [21]. Therefore, it is feasible to interconnect the mechanical properties of the different zones with f_{LAGB}. The f_{LAGBs} of QP BM, the sub-critical HAZ of QP side, DP BM and the sub-critical HAZ of DP side is exhibited in Figure 11e. The change of f_{LAGBs} is likely to be affected by tempering in welding. Dislocation accumulation more easily occurred in the LAGBs than that of the HAGBs, which led to significant dislocation interaction and formation of cracks. The f_{LAGBs} of the sub-critical HAZ of DP BM has the highest value, which indicates that cracks are more probably generated in this area under loading.

IPF, KAM and TF maps of the microstructure of the sub-critical HAZ in DP980 under different strains (0, 7.9% and 9.8% corresponding to unloaded, maximum load and onset of fracture, respectively) are presented in Figure 12. KAM map could illustrate the local strain distribution and indicate the dislocation density of the material [34]. The number of substructures and the KAM were improved as the increase of strain, as shown Figure 12a–f. Combined IPF map with KAM map, it is found that dislocation concentration occurred at grain boundaries. The value of TF can associate with the orientation-dependent hardness [35]. The grains with a lower TF value, such as 2.27, were associated with a lower yield strength, meaning the grains were "softer". Generally, a higher strain would produce higher TF value due to work hardening. Nevertheless, the grains with lower TF value (blue and green grains) throughout the deformation process could be observed, as shown Figure 12g–i. These softened grains played a significant role in delaying the damage and improving deformability of material [21, 36].

Figure 13a summarizes the relationship between strain of sub-critical HAZ of DP and average misorientation angle and f_{LAGBs}. With the increase of strain, the average

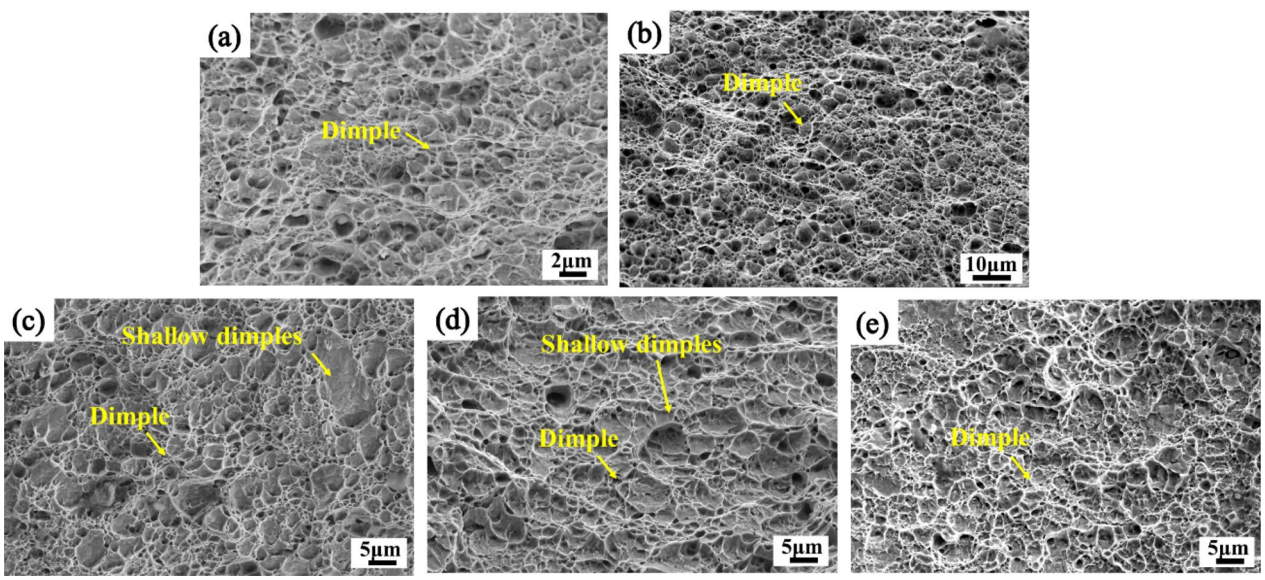

Figure 10 Micrograph of the fracture surface: **a** QP BM, **b** DP BM, **c** QP-DP joints, **d** DP-DP joints, **e** QP-QP joints

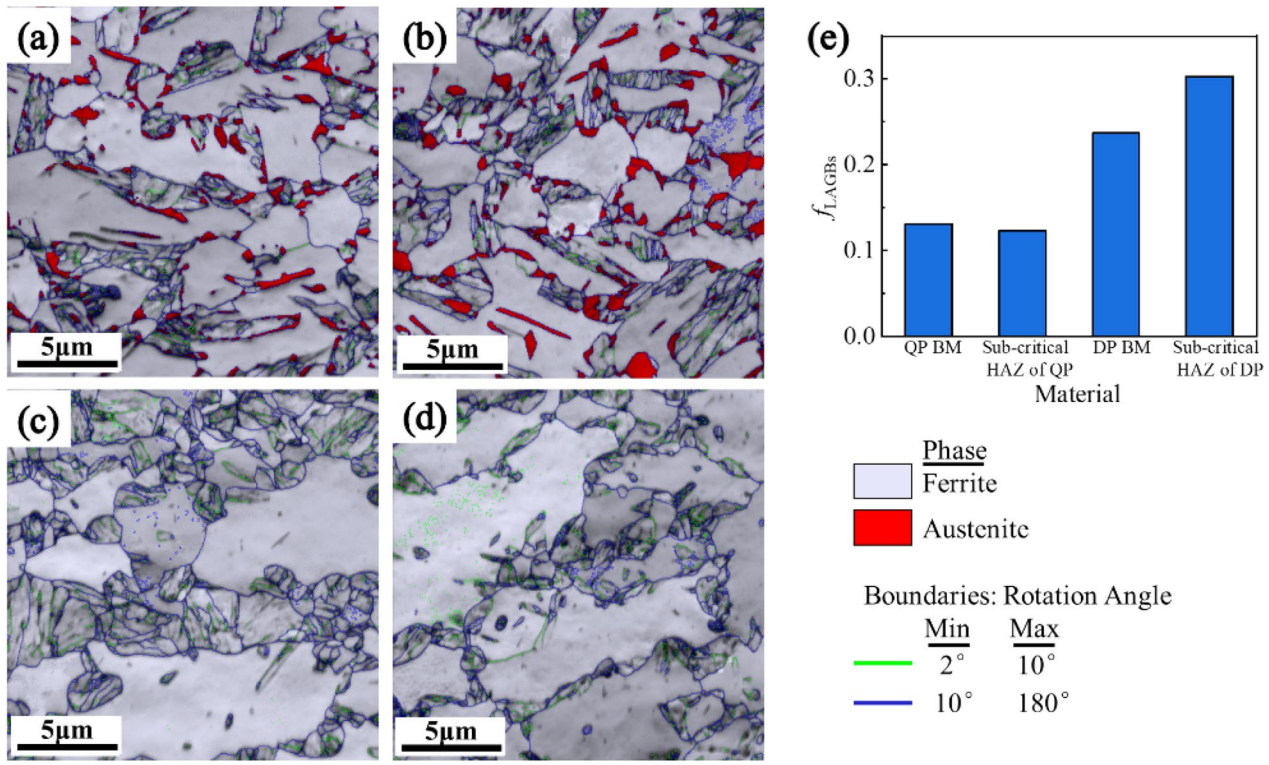

Figure 11 IQ map with phase: QP of **a** BM, **b** sub-critical HAZ; DP of **c** BM, **d** sub-critical HAZ and **e** the LAGBs fraction of QP BM, sub-critical HAZ of QP, DP BM and sub-critical HAZ of DP

misorientation angle reduced to 20.8° from 31.6°, and f_{LAGBs} increased from 0.24 to 0.5. Stress concentration occurred firstly at grain boundaries under loading, and grain boundaries generated dislocation. Therefore dislocation walls and slip bands were likely formed at the grain boundaries with the increase of strain, resulting in the formation of LAGBs. In addition, grain orientation could rotate under plastic deformation, which caused the misorientation of grains decrease and annihilation and rearrangement of substructures. Thus, it shows a low average misorientation angle and a high fraction of LAGBs [36].

The QP980-DP980 joint after maximum tensile load would begin necking in the sub-critical HAZ of DP side. KAM value and f_{LAGBs} in sub-critical HAZ of DP and QP side under maximum load are illustrated Figure 13b. KAM value and f_{LAGBs} in DP side were higher than that of QP. Extensive dislocation and a high percent of LAGBs made the strain concentration and necking appear in the sub-critical HAZ of DP side, confirming the sub-critical HAZ of DP side was the weakest area in the entire joint.

3.5 Biaxial Stretch Formability

Standard Erichsen cupping test can reflect the biaxial stretch formability of the welded joints. The Erichsen cupping test results of BM and welded joints are shown in Figure 14. The QP BM had the highest punch force (53.6 kN) and Erichsen value (10.6 mm). Because the QP contains RA, which was beneficial to delay crack propagation and increase the forming property [11, 37]. The WZ of all joints only included brittle martensite, which made the failure of welded joints initiate in WZ. Therefore, the joints had lower punch force and Erichsen value than that of BM. The Erichsen value (5.92 mm) of QP-DP joint was only 55.8% of BM of QP (10.6 mm), 60% of DP (9.87 mm), respectively, due to the different mechanical properties between QP980 and DP980 and their inhomogeneous deformation during test in joint.

The failure locations of Erichsen cupping test blanks of the similar and dissimilar welded joints are shown in Figure 15. The fracture surfaces of Erichsen cupping test blanks of the welded joints are illustrated in Figure 16. The dimples and quasi-cleavages were observed on the fracture surface of QP-DP joint (Figure 16b). This mixed fracture mode presented poor formability [22]. The fracture surfaces of similar welded joints indicated secondary cracks and dimples as shown in Figure 14b and c, especially a large number of dimples appeared on the fracture surface of QP-QP joint. The secondary crack can prevent propagation of the crack by reducing the stress concentration at the main crack tip [38, 39]. Therefore, the similar welded joints had better formability than dissimilar welded joint.

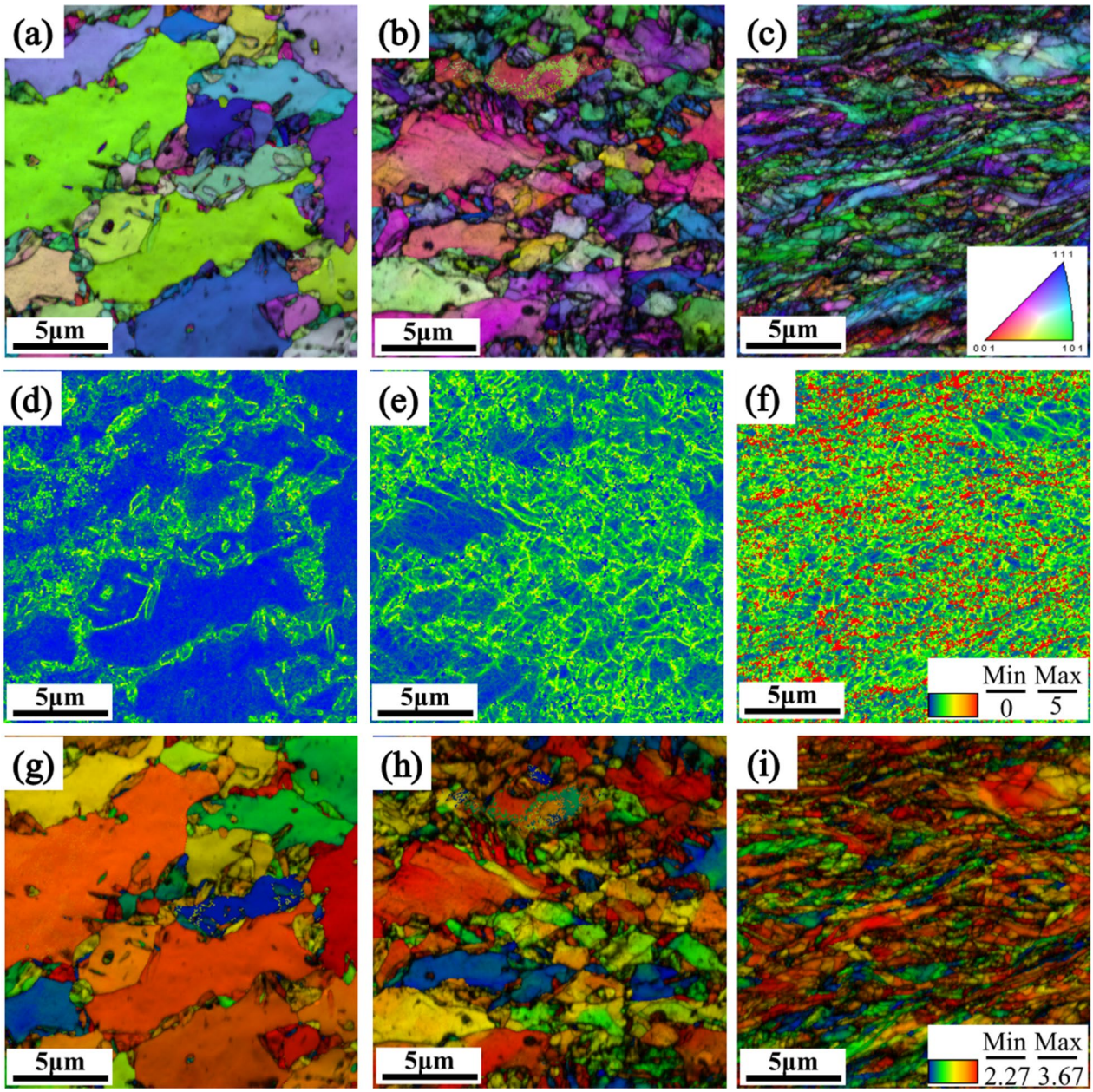

Figure 12 IPF, KAM and TF map of sub-critical HAZ of DP: **a**, **d**, **g** strain of 0; **b**, **e**, **h** strain of 7.9%; **c**, **f**, **i** strain of 9.8%

Erichsen value of the welded joints and BM was: 10.6 mm (QP980 BM) < 9.84 mm (DP980 BM) < 5.9 mm (QP-DP joint) < 6.6 mm (DP-DP joint) < 6.8 mm (QP-QP joint), as shown Figure 14b.

4 Conclusions

(1) The WZ of QP980-DP980 joint exhibited a higher microhardness (484.3 Hv) due to fully martensitic structure. The peak microhardness (549.5 Hv) appeared at the super-critical HAZ of QP980 side with finer martensite microstructure. The significant softening of the sub-critical HAZ of DP980 was observed.

(2) All dissimilar welded joints fractured at the sub-critical HAZ of DP980 side with a ductile fracture mode. Compared with DP980-DP980 joints, elongation and energy absorption of the QP980-DP980 welded joints increased by 36.7% and 36.9%.

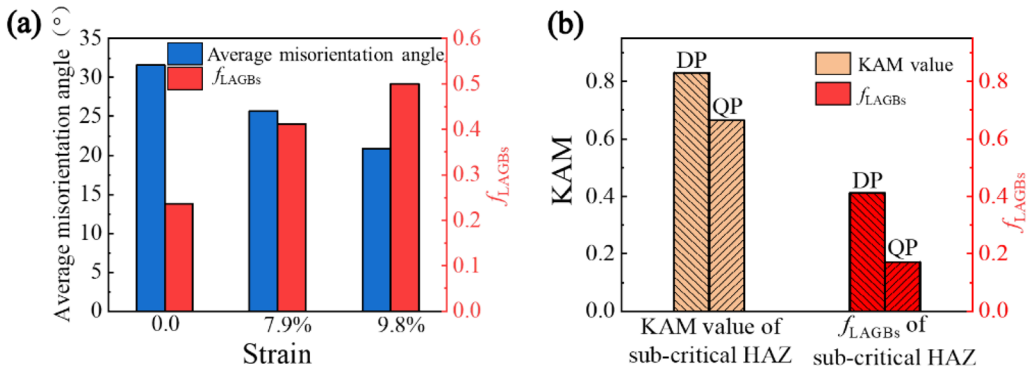

Figure 13 **a** The relationship between strain of sub-critical DP HAZ and average misorientation angle and f_{LAGBs}, **b** KAM value and f_{LAGBs} in sub-critical HAZ of DP BM and QP BM under maximum load

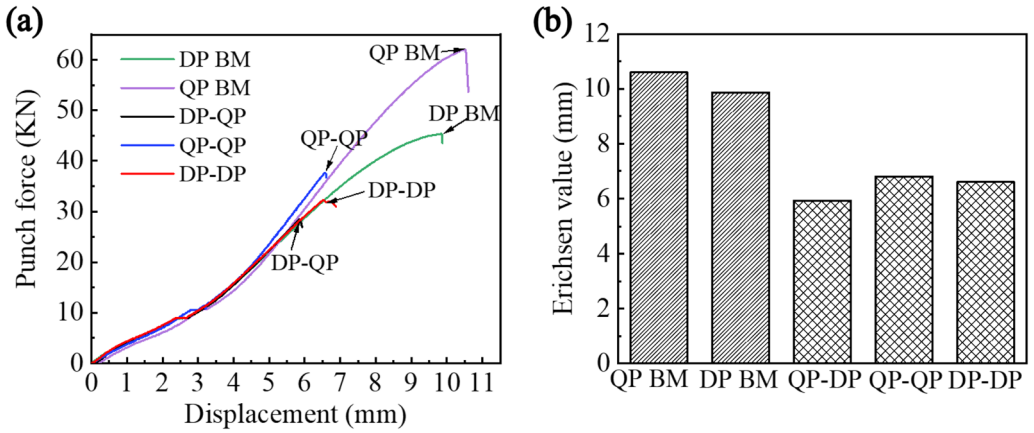

Figure 14 Erichsen cupping test results of base metal and welded blanks: **a** Punch force and displacement curves and **b** Erichsen values

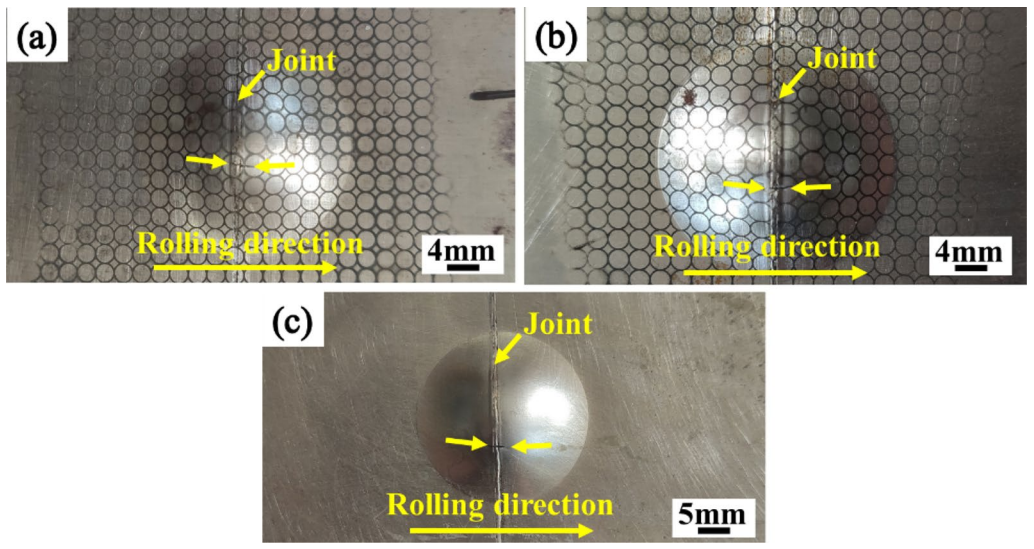

Figure 15 Failure locations of Erichsen cupping test blanks of joints: **a** QP-DP joint, **b** QP-QP joint and **c** DP-DP joint

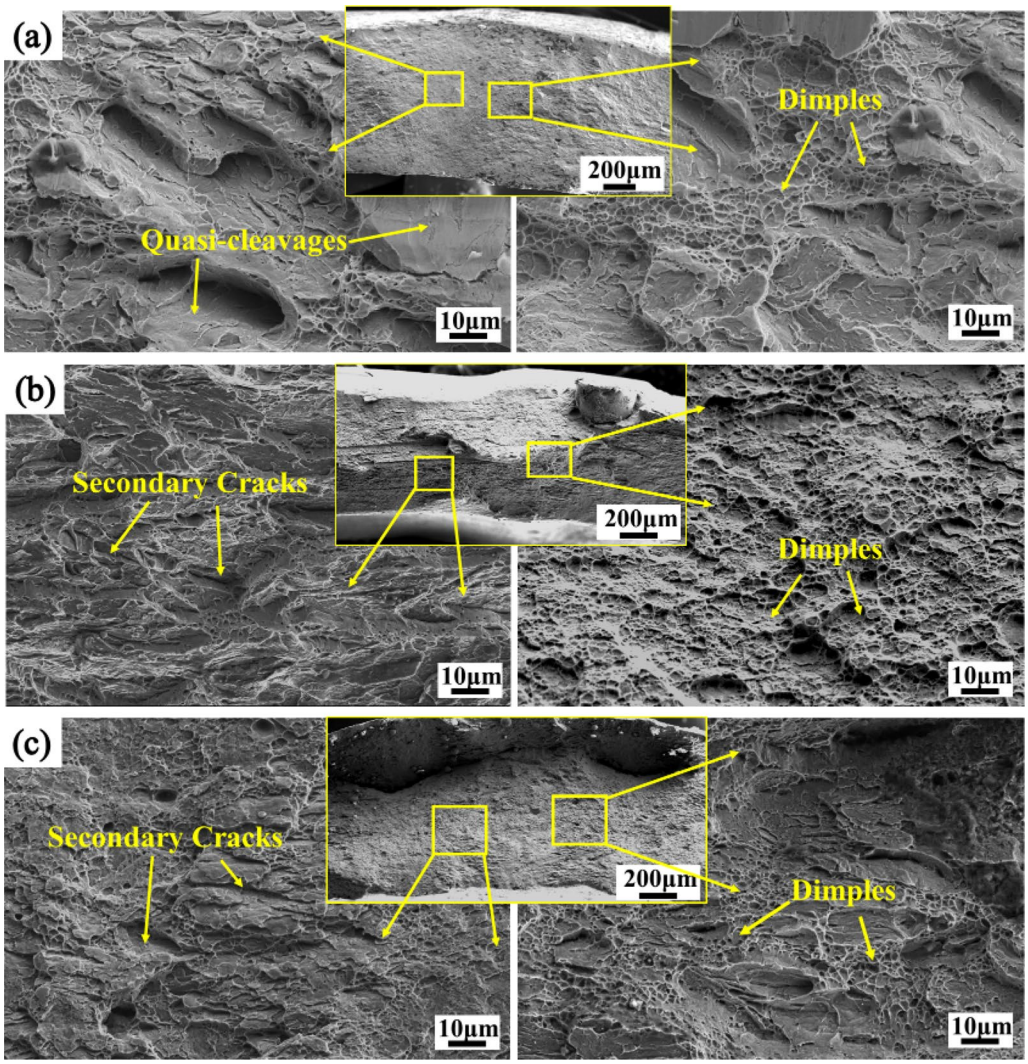

Figure 16 Fracture surfaces of Erichsen cupping test blanks of joints: **a** QP-DP joint, **b** QP-QP joint and **c** DP-DP joint

(3) The LAGBs fraction of the sub-critical HAZ of DP980 side was higher in unloaded and at maximum load stage. It proved that the sub-critical HAZ of DP980 side was the weakest area in the entire joint. With the increase of strain, the LAGBs fraction, the number of substructures and KAM value of the sub-critical HAZ of DP980 side were improved while the average misorientation angle reduced due to the motion, rearrangement and annihilation of dislocation.

(4) Erichsen test of the dissimilar welded joints failed at the WZ. The Erichsen values (5.92 mm) and the maximum punch force (28.4 kN) of QP980-DP980 joints significantly decreased compared with that of DP980 BM. The mixed fracture mode including the dimples and quasi-cleavages was observed on the fracture surfaces of the dissimilar welded joints.

Acknowledgements
Not applicable.

Authors' Contributions
JX, PP and WG conceived and designed. MX, CT and YL provided the experimental materials and test equipment. JX wrote the paper. JX, ZW and HZ reviewed and edited the manuscript. All authors read and approved the final manuscript.

Authors' Information
Junliang Xue is a PhD student at *School of Mechanical Engineering and Automation, Beihang University, China*. His research interests include laser welding and brazing.

Peng Peng is a teacher at *Beihang University, China*. His research interests include welding and nano-micro joining.

Wei Guo is a teacher at *Beihang University, China*. He received his doctor degree from *Jilin University, China*. His research interests include welding, nano-micro joining and laser shock processing.

Mingsheng Xia is a senior expert of *TANGSTEEL Company, China*. His research interests include advanced high strength steel manufacturing and joining.

Caiwang Tan is a teacher at *Harbin Institute of Technology at Weihai, China*. He received his doctor degree from *Harbin Institute of Technology, China*. His research interests include welding and joining.

Zhandong Wan is a PhD student at *Tsinghua University, China*. His research interests include AHSSs laser welding and laser shock processing.

Hongqiang Zhang is a teacher at *Beihang University, China*. He received his doctor degree from *Tsinghua University, China*. His research interests include welding and laser shock processing.

Yongqiang Li is a teacher at *Changchun automobile industry institute, China*. He received his doctor degree from *Jilin University, China*. His research interests include AHSSs welding.

Funding
Supported by National Natural Science Foundation of China (Grant Nos. 51871010, 51875129), and Beijing Municipal Natural Science Foundation of China (Grant No. 3202016 3212008).

Competing Interests
The authors declare no competing financial interests.

Author Details
[1]School of Mechanical Engineering and Automation, Beihang University, Beijing 100191, China. [2]R&D Center, TANGSTEEL Company, HBIS Group, Tangshan 063016, China. [3]Shandong Provincial Key Laboratory of Special Welding Technology, Harbin Institute of Technology at Weihai, Weihai 264209, China. [4]Department of Mechanical Engineering, Tsinghua University, Beijing 100084, China. [5]Electrical Engineering Department, Changchun Automobile Industry Institute, Changchun 130013, China.

Received: 20 March 2020 Revised: 19 April 2021 Accepted: 16 July 2021
Published online: 28 August 2021

References

[1] S Curtze, V T Kuokkala, M Hokka, et al. Deformation behavior of TRIP and DP steels in tension at different temperatures over a wide range of strain rates. *Mat. Sci. Eng. A-Struct.*, 2009, 507(1-2): 124-131.
[2] J F Wang, L J Yang, M S Sun, et al. Effect of energy input on the microstructure and properties of butt joints in DP1000 steel laser welding. *Materials & Design*, 2016, 90: 642-649.
[3] J G Speer, F C R Assunção, D K Matlock, et al. The "quenching and partitioning" process: background and recent progress. *Materials Research*, 2005, 8(4): 417-423.
[4] J Speer, D K Matlock, B C De Cooman, et al. Carbon partitioning into austenite after martensite transformation. *Acta Mater*, 2003, 51(9): 2611–2622.
[5] S Yan, X H Liu, W J Liu, et al. Comparative study on microstructure and mechanical properties of a C-Mn-Si steel treated by quenching and partitioning (Q & P) processes after a full and intercritical austenitization. *Mat. Sci. Eng. A-Struct.*, 2017, 684: 261–269.
[6] P J Jacques, Q Furnémont, F Lani, et al. Multiscale mechanics of TRIP-assisted multiphase steels: I. Characterization and mechanical testing. *Acta Mater.*, 2007, 55(11): 3681–3693.
[7] W S Li, H Y Gao, H Nakashima, et al. In-situ study of the deformation-induced rotation and transformation of retained austenite in a low-carbon steel treated by the quenching and partitioning process. *Mat. Sci. Eng. A-Struct.*, 2016, 649: 417–425.
[8] W Guo, Z Wan, Q Jia, et al. Laser weldability of TWIP980 with DP980/B1500HS/QP980 steels: Microstructure and mechanical properties. *Optics & Laser Technology*, 2020, 124: 105961.
[9] J J Guzman-Aguilera, C J Martinez-Gonzalez, V H Baltazar-Hernandez, et al. Influence of SC-HAZ microstructure on the mechanical behavior of Si-TRIP steel welds. *Materials Science and Engineering: A*, 2018, 718: 216–227.
[10] N Farabi, D L Chen, Y Zhou. Microstructure and mechanical properties of laser welded dissimilar DP600/DP980 dual-phase steel joints. *J. Alloy Compd.*, 2011, 509(3): 982–989.
[11] W Li, L Ma, P Peng, et al. Microstructural evolution and deformation behavior of fiber laser welded QP980 steel joint. *Materials Science and Engineering: A*, 2018, 717: 124-133.
[12] Y M Sun, L J Wu, C W Tan, et al. Influence of Al-Si coating on microstructure and mechanical properties of fiber laser welded 22MnB5 steel. *Opt. Laser Technol.*, 2019, 116: 117-127.
[13] L Zhou, Z Y Li, X G Song, et al. Influence of laser offset on laser welding-brazing of Al/brass dissimilar alloys. *J. Alloy Compd.*, 2017, 717: 78–92.
[14] H W Yang, Y M Sun, C W Tan, et al. Influence of Al-Si coating on microstructure and mechanical properties of fiber laser welded and then press-hardened 22MnB5 steel. *Mat. Sci. Eng. A-Struct.*, 2020, 794: 139918.
[15] W Guo, Z Wan, P Peng, et al. Microstructure and mechanical properties of fiber laser welded QP980 steel. *Journal of Materials Processing Technology*, 2018, 256: 229-238.
[16] S Nemecek, T Muzik, M Misek. Differences between laser and arc welding of HSS steels. *Physcs Proc.*, 2012, 39: 67-74.
[17] X N Wang, Q Sun, Z Zheng, et al. Microstructure and fracture behavior of laser welded joints of DP steels with different heat inputs. *Mat. Sci. Eng. A-Struct.*, 2017, 699: 18-25.
[18] A P Pierman, O Bouaziz, T Pardoen, et al. The influence of microstructure and composition on the plastic behaviour of dual-phase steels. *Acta Mater.*, 2014, 73: 298-311.
[19] G K Ahiale, Y J Oh, Microstructure and fatigue performance of butt-welded joints in advanced high-strength steels. *Materials Science & Engineering A*, 2014, 597: 342-348.
[20] R S Sharma, P Molian. Yb:YAG laser welding of TRIP780 steel with dual phase and mild steels for use in tailor welded blanks. *Materials & Design*, 2009, 30(10): 4146-4155.
[21] N Saeidi, F Ashrafizadeh, B Niroumand, et al. EBSD study of micromechanisms involved in high deformation ability of DP steels. *Materials & Design*, 2015, 87: 130–137.
[22] Q Jia, W Guo, Z Wan, et al. Microstructure and mechanical properties of laser welded dissimilar joints between QP and boron alloyed martensitic steels. *Journal of Materials Processing Technology*, 2018, 259: 58-67.
[23] Q L Cui, D Parkes, D Westerbaan, et al. Tensile and fatigue properties of single and multiple dissimilar welded joints of DP980 and HSLA. *Journal of Materials Engineering & Performance*, 2017, 26(2): 1-9.
[24] D Parkes, W Xu, D Westerbaan, et al. Microstructure and fatigue properties of fiber laser welded dissimilar joints between high strength low alloy and dual-phase steels. *Materials & Design*, 2013, 51: 665-675.
[25] V H B Hernandez, S S Nayak, Y Zhou. Tempering of martensite in dual-phase steels and its effects on softening behavior. *Metall Mater Trans A*, 2011, 42a(10): 3115-3129.
[26] Q Jia, W Guo, W D Li, et al. Experimental and numerical study on local mechanical properties and failure analysis of laser welded DP980 steels. *Mat. Sci. Eng. A-Struct.*, 2017, 680: 378-387.
[27] J H Lee, S H Park, H S Kwon, et al. Laser, tungsten inert gas, and metal active gas welding of DP780 steel: Comparison of hardness, tensile properties and fatigue resistance. *Materials & Design*, 2014, 64(9): 559-565.
[28] S Sadeghpour, S M Abbasi, M Morakabati, et al. A new multi-element beta titanium alloy with a high yield strength exhibiting transformation and twinning induced plasticity effects. *Scripta Mater.*, 2018, 145: 104-108.
[29] B Hutchinson, N Ridley. On dislocation accumulation and work hardening in Hadfield steel. *Scripta Mater.*, 2006, 55(4): 299-302.
[30] H Rastegari, A Kermanpur, A Najafizadeh. Effect of initial microstructure on the work hardening behavior of plain eutectoid steel. *Mat. Sci. Eng. A-Struct.*, 2015, 632: 103–109.
[31] Q G Li, X F Huang, W G Huang, Microstructure and mechanical properties of a medium-carbon bainitic steel by a novel quenching and dynamic partitioning (Q-DP) process. *Mat. Sci. Eng. A-Struct.*, 2016, 662: 129–135.
[32] G Mandal, S K Ghosh, S Bera, et al. Effect of partial and full austenitisation on microstructure and mechanical properties of quenching and partitioning steel. *Mat. Sci. Eng. A-Struct.*, 2016, 676: 56-64.

[33] N Farabi, D L Chen, J Li, et al. Microstructure and mechanical properties of laser welded DP600 steel joints. *Materials Science and Engineering: A*, 2010, 527(4-5): 1215-1222.
[34] S I Wright, M M Nowell, D P Field. A review of strain analysis using electron backscatter diffraction. *Microsc Microanal*, 2011, 17(3): 316-329.
[35] M R Stoudt, L E Levine, A Creuziger, et al. The fundamental relationships between grain orientation, deformation-induced surface roughness and strain localization in an aluminum alloy. *Mat. Sci. Eng. A-Struct.*, 2011, 530: 107–116.
[36] S C Li, C Y Guo, L L Hao, et al. In-situ EBSD study of deformation behaviour of 600 MPa grade dual phase steel during uniaxial tensile tests. *Mat. Sci. Eng. A-Struct.*, 2019, 759: 624–632.
[37] I D Diego-Calderón, M J Santofimia, J M Molina-Aldareguia, et al. Deformation behavior of a high strength multiphase steel at macro- and micro-scales. *Materials Science & Engineering A*, 2014, 611(9): 201-211.
[38] J Yang, T S Wang, B Zhang, et al. High-cycle bending fatigue behaviour of nanostructured bainitic steel. *Scripta Mater.*, 2012, 66(6): 363–366.
[39] Q G Li, X F Huang, W G Huang. EBSD analysis of relationship between microstructural features and toughness of a medium-carbon quenching and partitioning bainitic steel. *J. Mater. Eng. Perform.*, 2017, 26(12): 6149-6157.